

Simulation Model of Reactive Nitrogen Species in an Urban Atmosphere using a Deep Neural Network: RNDv1.0

Junsu Gil¹, Meehye Lee^{1*}, Jeonghwan Kim², Gangwoong Lee², Joonyoung Ahn³, Cheol-hee Kim⁴

¹ Department of Earth and Environmental Sciences, Korea University, Seoul, South Korea

² Department of Environmental Science, Hankuk University of Foreign Studies, Yongin, South Korea

³ Air Quality Forecasting Center, Climate and Air Quality Research Department, National Institute of Environmental Research (NIER), Incheon, South Korea

⁴ Department of Atmospheric Science, Pusan National University, Busan, South Korea

* Corresponding author: Meehye Lee (meehye@korea.ac.kr)

Abstract

Nitrous acid (HONO), one of the reactive nitrogen oxides (NO_y), plays an important role in the formation of ozone (O₃) and fine aerosols (PM_{2.5}) in the urban atmosphere. In this study, a new simulation approach to calculate HONO mixing ratios using a deep neural technique based on measured variables was developed. The 'Reactive Nitrogen species simulation using Deep neural network (RND)' has been implemented in Python. The first version of RND (RNDv1.0) was trained, validated, and tested with HONO measurement data obtained in Seoul during the warm months from 2016 to 2019.

A k-fold cross validation and test results confirmed the performance of RND v1.0 with an Index Of Agreement (IOA) of 0.79 ~ 0.89 and a Mean Absolute Error (MAE) of 0.21 ~ 0.31 ppbv. The RNDv1.0 adequately represents the main characteristics of the measured HONO and thus, RND v1.0 is proposed as a supplementary model for calculating the HONO mixing ratio in a polluted urban environment.

1. Introduction

Surface ozone (O_3) pollution has been reported to be worsen over continental areas (Arnell et al., 2019; Monks et al., 2015; Varotsos et al., 2013; IPCC, 2014). In particular, a warmer climate is expected to increase surface O_3 concentrations and peak levels in polluted regions, depending on its precursor levels (IPCC 2021). As one of the short-lived climate pollutants (SLCPs), O_3 also interacts with the global temperature via positive feedback (Shindell et al., 2013; Myhre et al., 2017; Stevenson et al., 2013). Therefore, it is imperative to accurately predict the mixing ratios and variations of surface O_3 . While operational models such as community multiscale air quality (CMAQ) have been used widely for this purpose, uncertainties still arise from poorly understood chemical mechanisms involving reactive nitrogen oxides (NO_y) and volatile organic compounds (VOCs), and lack of their measurements (Mallet and Sportisse, 2006; Canty et al., 2015; Akimoto et al., 2019; Shareef et al., 2019; Cheng et al., 2022).

In the urban atmosphere, NO_y typically includes NO_x ($NO + NO_2$), HONO, HNO_3 , organic nitrates (e.g., PAN), NO_3 , N_2O_3 , and particulate NO_3^- . These species are produced and recycled through photochemical reactions until they are removed through wet or dry deposition (Liebmann et al., 2018; Brown et al., 2017; Wang et al., 2020; Li et al., 2020). NO_y play an important role in critical environmental issues concerning the Earth's atmosphere, spanning from local air pollution to global climate change (Sun et al., 2011; Ge et al., 2019). The oxidation of NO to NO_2 , and finally to HNO_3 , is the backbone of the chemical mechanism producing ozone (O_3) and $PM_{2.5}$ (particulate matter of size $\leq 2.5 \mu m$), and it determines the oxidization capacity of the atmosphere. Recently, as O_3 has increased along with a decrease in NO_x emission over many regions including East Asia, interest in the heterogeneous reaction of reactive nitrogen oxides, which is yet to be understood, has been newly raised (Brown et al., 2017; Stadtler et al., 2018). Currently, the lack of measurement of individual NO_y species hindered a comprehensive understanding of the heterogeneous reactions (Anderson et al., 2014; Wang et al., 2017b; Chen et al., 2018b; Akimoto and Tanimoto, 2021; Stadtler et al., 2018).

In particular, there are growing number of evidence for heterogeneous formation of HONO in relation to high $PM_{2.5}$ and O_3 occurrence in urban areas (e.g., (Li et al., 2021b). As

61 an OH reservoir, HONO will expedite the photochemical reactions involving VOCs and NOx
62 in the early morning, leading to O₃ and fine aerosol formation. Nonetheless, its formation
63 mechanism has not been elucidated clearly enough to be constrained in conventional
64 photochemical models. In addition to the reaction of NO with OH (Bloss et al., 2021), various
65 pathways of HONO formation have been suggested from laboratory experiments, field
66 measurements, and model simulations: direct emissions from vehicles (e.g., (Li et al., 2021a)
67 and soil (e.g.,(Bao et al., 2022), photolysis of particulate nitrate (e.g., (Gen et al., 2022),
68 heterogeneous conversion of NO₂ on various aerosol surfaces (e.g., (Jia et al., 2020), ground
69 surface (e.g.,(Meng et al., 2022), and microlayers of sea surface (e.g., (Gu et al., 2022). Among
70 these, the heterogeneous reaction mechanism on the surface is of major interest in the recent
71 HONO study.

72 HONO has been measured mostly during intensive campaigns in urban areas using
73 various techniques such as a long path absorption photometer (LOPAP) (Kleffmann et al.,
74 2006;Xue et al., 2019), chemical ionization mass spectrometry (CIMS) (Levy et al.,
75 2014;Roberts et al., 2010), ion chromatography (IC) (VandenBoer et al., 2014;Gil et al.,
76 2020;Ye et al., 2016;Xu et al., 2019), and quantum cascade tunable infrared laser differential
77 absorption spectrometry (QC-TILDAS) (Lee et al., 2011;Gil et al., 2021). Of these methods,
78 QC-TILDAS has served as a reference for intercomparison of measurement data from different
79 techniques due to high time resolution and stability (Pinto et al., 2014). These studies reported
80 the maximum HONO of several ppb levels at nighttime. In comparison, the model captured at
81 most 67~90 % of the observed HONO in megacities such as Beijing (Tie et al., 2013;Liu et al.,
82 2019).

83 In recent years, Machine Learning (ML) method has been adopted in the atmospheric
84 science for pattern classification (e.g. New Particle Formation event) and forecasting and
85 spatiotemporal modelling of O₃ and PM_{2.5} (Arcomano et al., 2021;Shahriar et al.,
86 2020;Krishnamurthy et al., 2021;Cui and Wang, 2021;Joutsensaari et al., 2018;Chen et al.,
87 2018a;Kang et al., 2021). Among ML methods, the Neural Network (NN) architecture is widely
88 used owing to its powerful ability to process large amounts of data, allowing improvement in
89 the performance of conventional models through being integrated with physical equations
90 (Reichstein et al., 2019;Schultz et al., 2021). As a NN architecture, a multi-layer artificial neural
91 network, referred to as a Deep Neural Network (DNN), employs a statistical method that learn

92 non-linear relations in data and obtain the optimum solution for the target species without prior
93 information on the physicochemical processes. DNN has advantages over other NN architecture
94 such as Convolution NN (CNN) or Long-Short Term Memory (LSTM) because it works well
95 for discrete spatiotemporal data. In general, the performance of DNN is similar to or better than
96 other ML methods for small number of data as well as large data set (Baek and Jung, 2021; Dang
97 et al., 2021; Sumathi and Pugalendhi, 2021).

98 When the DNN method is applied to atmospheric chemical constituents, it requires
99 large amount of data for training and thus, the size of measurement data becomes a limiting
100 factor for trace species such as HONO, which are not routinely measured such as O₃ or PM_{2.5}.
101 In this regard, the daily average HONO mixing ratio was attempted to be estimated using
102 ensemble ML models with satellite measurements (Cui and Wang, 2021). In comparison, the
103 hourly HONO mixing ratio was calculated using a simple NN architecture with measured
104 variables, which were thought to be deeply involved in the formation of HONO (Gil et al.,
105 2021). The accuracy of the hourly HONO estimated from input variables such as aerosol surface
106 areas and mixed layer height was better than the daily HONO estimate.

107 The aim of this study is to develop a user-friendly ‘Reactive Nitrogen species simulation using
108 DNN’ model (RNDv1.0) that estimates HONO mixing ratios from real-time measurements of
109 criteria pollutants and meteorological parameters and is ultimately to be incorporated into
110 operational models that forecast urban air quality. Since this study is the first attempt to
111 calculate the HONO mixing ratio using RNDv1.0, the entire construction process is described
112 in detail, and the performance is evaluated by comparing the results with simulations using a
113 commonly used model and observations over several years.

114

115 **2. Model description**

116

117 The development of RNDv1.0 model follows the systematic steps similar to a general
118 machine learning model construction workflow, including collecting data, preprocessing data,
119 building the DNN, training and validating the model, and testing the performance of the model
120 (Figure 1). The RNDv1.0 was written in Python and necessary libraries to build and operate

121 RNDv1.0 are listed in Table 1. The dataset used to train-test-validation can be downloaded from
122 Gil et al., 2021.

123

124 **2.1. Collection of measurement data for model construction**

125

126 As the first step constructing the RNDv1.0, measurement data were obtained including
127 HONO, reactive gases, and meteorological parameters. It is noteworthy that the HONO
128 measurement data is for model construction and is not required to run the RND model. The
129 HONO mixing ratio was measured using a Quantum Cascade – Tunable Infrared Laser
130 Differential Absorption Spectrometer (QC-TILDAS) system in Seoul during May–June 2016,
131 June 2018, and April–June 2019 (Lee et al., 2011; Gil et al., 2021). When testing and evaluating
132 atmospheric HONO measurement methods, QC-TILDAS has been chosen as the reference
133 method for comparing ambient HONO mixing ratios measured using several different
134 techniques owing to its advantages of low detection limits (~ 0.1 ppbv) and high temporal
135 resolution (Pinto et al., 2014). More details on measurements can be found elsewhere (Gil et
136 al., 2021).

137 HONO was measured at Olympic Park (37.52°N , 127.12°E) during the Korea-United
138 States Air Quality (KORUS-AQ) study in 2016 (Kim et al., 2020; Gil et al., 2021), at the campus
139 of Korea University (37.59°N , 127.03°E) in 2018, and at the site near the campus (37.59°N ,
140 127.08°E) in 2019 (NIER, 2020) (Figure S1). Although measurements were made at three sites,
141 O_3 and $\text{PM}_{2.5}$ levels have been known to be greatly influenced by the synoptic circulation
142 throughout the Korean peninsula (Peterson et al., 2019; Jordan et al., 2020), and the Korea
143 University campus and Olympic Park have served as measurement sites representing the air
144 quality of Seoul. In addition to HONO, trace gases including O_3 , NO_2 , CO , and SO_2 and
145 meteorological parameters including temperature (T), relative humidity (RH), wind speed (WS)
146 and direction (WD) were measured. Note that HONO was not significantly correlated with any
147 of these variables (Figure S2). The measurement statistics are presented in Table 2 and Table
148 S1. Briefly summarizing, the 10th and 90th percentile mixing ratios of HONO, NO_2 , and O_3 are
149 0.3 ppbv and 1.9 ppbv, 10.7 ppbv and 48.2 ppbv, and 12.0 ppbv and 80.9 ppbv, respectively for
150 the entire experiment periods.

151

152 **2.2. Data preprocessing**

153

154 In the next step, the observation data set was prepared for RNDv1.0 model construction.
155 As input variables, hourly measurements of chemical and meteorological parameters are used,
156 including the mixing ratios of O₃, NO₂, CO, and SO₂, along with temperature (T), relative
157 humidity (RH), wind speed (WS), wind direction (WD), and solar zenith angle (SZA) to
158 estimate the target species, HONO, as the output. Wind direction in degrees were converted to
159 a cosine value for continuity. As a last step in data processing, missing values were filtered out
160 from the input dataset. Finally, 50.7 % of all available measurement data (1636) were used to
161 construct the RNDv1.0 in this study.

162 Since the measurements of these nine variables vary over a wide range in different units,
163 they were normalized to avoid bias during the calculations. Among the widely used
164 normalization methods, ‘*min-max scaling*’ method was adopted and input variables were
165 normalized against the minimum and maximum values in this study (Eq. 1):

166

$$167 \quad x_{\text{sca}} = \frac{x_{\text{raw}} - F_2(X)}{F_1(X)}, \quad (1)$$

168

169 where x_{raw} is raw data, x_{sca} is scaled value, and F_1 and F_2 are scale factors of input
170 variable (X), which are listed in Table 2.

171

172 **2.3. Neural network architecture and hyperparameters**

173

174 At this stage, the network is built to calculate HONO using those input variables. The
175 RNDv1.0 is composed of five hidden layers (Figure 2), which employed an exponential linear
176 unit (ELU) as an activation function (Eq. 2).

177

178
$$\text{ELU} : \phi(x) = \begin{cases} e^x - 1 & (x < 0) \\ x & (x \geq 0) \end{cases}. \quad (2)$$

179

180 In a DNN, an activation function creates a nonlinear relationship between an input
 181 variable and an output variable. When constructing a DNN model, an ELU has the advantage
 182 of a fast-training process and better performance in handling negative values than other
 183 activation functions (Wang et al., 2017a;Ding et al., 2018). In addition, the mean squared error
 184 and Adam optimizer were applied as loss function and optimize function, respectively. The
 185 learning rate, epoch, and batch were set to 0.01, 100, and 32, respectively.

186

187 **2.4. Model training**

188

189 The RNDv1.0 model was trained, validated, and tested with HONO measurements obtained
 190 during May ~ June in 2016 and 2019, in June 2018, and in April 2019, respectively (Figure 3).
 191 The number of data used for train, validation, and test were 1122, 381, and 133, respectively.

192 With the hyperparameters specified in previous section, the performance of the model was
 193 firstly validated using the k-fold cross-validation method, which is especially useful when the
 194 size of dataset is small (Bengio and Grandvalet, 2003). In the k-fold cross-validation method
 195 (Figure 3), the entire data is randomly divided into k subsets, of which k-1 sets were used for
 196 training and the rest one was used for validation. k was set to 5 in this study. The accuracy was
 197 determined by Index Of Agreement (IOA) and Mean Absolute Error (MAE) expressed by the
 198 following equation (Eq. 3, Eq. 4):

199

200
$$\text{IOA} = 1 - \frac{\sum_{i=1}^n (O_i - P_i)^2}{\sum_{i=1}^n (|P_i - \bar{O}| + |O_i - \bar{O}|)^2}, \quad (3)$$

201
$$\text{MAE} = \frac{\sum_{i=1}^n |O_i - P_i|}{n}, \quad (4)$$

202

203 where O_i , P_i , \bar{O} , and n are the observed value, predicted value, average of the observed
 204 values, and number of nodes, respectively. The overall accuracy of

205 As IOA and MAE vary according to the number of nodes, they were calculated for the
206 measured (HONO_{obs}) and calculated (HONO_{mod}) mixing ratios by varying the number of nodes
207 from 0 to 100 in each hidden layer. The best performance was found with 41 nodes, with which
208 the averaged IOA and MAE were 0.89 ± 0.01 (mean \pm standard deviation) and 0.31 ± 0.02 ppbv,
209 respectively (Figure 4). The high level of IOA and low MAE demonstrates that the performance
210 of RNDv1.0 model is adequate, and it is capable of simulating the ambient HONO mixing ratio
211 using the routinely measured criteria pollutants and meteorological parameters. In particular,
212 MAE was commensurate with the detection limit of HONO measurement.

213 After the network validation, HONO mixing ratio was calculated for May ~ June in 2016
214 and 2019, and the model results were compared with the measured values (Figure 5). The
215 average mixing ratios of measured and calculated HONO was 0.94 ppbv and 0.89 ppbv in 2016,
216 and 1.02 ppbv and 0.96 ppbv in 2019, respectively. The MAE and IOA of the measurement and
217 calculation were 0.27 ppbv and 0.90 in 2016, and 0.29 ppbv and 0.91 in 2019, respectively,
218 demonstrating the ability of the RNDv1.0 to simulate ambient HONO levels. In both cases,
219 however, the model slightly underestimated the highest and lowest HONO mixing ratios, which
220 is mainly due to the limited number of data used for training, but also related to the intrinsic
221 nature of DNN. The model calculation well captured the diurnal variation of ambient HONO
222 with a slight underestimation (Figure 6). In addition, the correlation between HONO_{mod} and
223 HONO_{obs} was better in 2019 (MAE = 0.06 ppbv) than in 2016 (MAE = 0.08 ppbv). Since the
224 MAE of the two cases was far below the detection limit of HONO measurements (~ 0.1 ppbv),
225 the RNDv1.0 is considered suitable for simulating HONO in urban areas.

226 Next, the HONO calculated in RNDv.1.0 was compared with observations and results from
227 CMAQ (Community Multi-scale Air Quality Model, v5.3.1) simulations during the KORUS-
228 AQ study (May~June 2016) (Figure 7). More information on CMAQ modeling can be found
229 elsewhere (Appel et al., 2021). While the results of RNDv.1.0 reasonably traced the observed
230 variations (IOA = 0.90), the CMAQ severely underestimated the measured HONO
231 concentration (IOA = 0.44). These results demonstrate the performance and efficacy of
232 RNDv1.0 in calculating the ambient HONO mixing ratio that are poorly reproduced in
233 conventional operating models.

234

235 **2.5. Influence of input variables on HONO concentration**

236

237 A simple bootstrapping test was conducted to evaluate the relative importance of the input
238 variable to HONO concentration. In this analysis, each variable was set to zero and MAE was
239 calculated as an evaluation metrics (Kleinert et al., 2021). Of nine input variables, NO₂ was
240 found to have the most significant influence on HONO concentration, followed by RH,
241 temperature, and solar zenith angle (Table 4). The highest MAE of 0.59 ppbv can be considered
242 as the maximum uncertainty of RNDv1.0 due to the input variable.

243 The result of bootstrap test is in good agreement with those of our previous study (Gil et
244 al., 2021), where more variables such as aerosol surface area and mixing layer height were
245 incorporated into the model, highlighting the crucial role of precursor gases and heterogeneous
246 conversion in HONO formation. Therefore, these results demonstrate that the RND model
247 constructed from routinely measured criteria pollutants and meteorological parameters
248 sufficiently captured the HONO variability in the urban atmosphere.

249

250 **2.6. Model validation and test**

251

252 Finally, the RND model was validated and tested against the measurement data obtained in
253 June 2018 and April 2019. The calculated HONO mixing ratios are compared with those
254 measured in Figure 8, and their MAE and IOA are listed in Table 3. The two sets of model
255 performance test showed that the model reasonably traced what was observed. As the validation
256 result of RND, the MAE and IOA of the calculated and measured in June 2018 are comparable
257 to those of 2016~2019 result. However, the MAE and IOA of the April 2019 measurements
258 were relatively poor compared to the validation results. Especially, the MAE of the April 2019
259 is about twice as high as those of validation.

260 In these two test periods, HONO levels were lower than those observed on validation days
261 (Figure 8), and the model tended to overestimate high HONO concentrations. It is possibly due
262 to the variability of HONO that is not fully captured by RNDv1.0 using 9 input variables. As
263 stated above, heterogeneous reactions intimately involved in HONO formation are not
264 considered in RNDv1.0. More importantly, the annual variability of criteria pollutants such as

265 PM_{2.5} has increased in recent years. Particularly in 2019, the monthly average PM_{2.5} mass
266 concentration was lower in April (21 µg m⁻³) than in May (29 µg m⁻³), unlike normal years.
267 Given that the test result is within the uncertainty range of the model that is primarily
268 determined by NO₂ (Table 4), RNDv1.0 will be applicable to urban environments under various
269 conditions.

270

271 **3. Operation and application of RNDv1.0**

272

273 The RNDv1.0 package is provided as an operational model, .h5 files that can be opened in
274 Python. To run the RNDv1.0, the measurement data for nine input variables are required and
275 need to be properly prepared as described in Section 2.2. A sample of preprocessed input dataset
276 is provided as a .csv file (Dataset_for_model.csv). Once the input data is ready, open the
277 RNDv1.0 with input data files using the code provided in the example (Figure S3). Then, RND
278 v1.0 calculates and presents the HONO results as scaled values (x_{sca}), which will be finally
279 converted to HONO mixing ratio (ppbv) by the two scale factors in Table 2 (Eq. 5):

280

$$281 \quad \text{HONO (ppbv)} = \text{HONO}_{sca} \times F_1(\text{HONO}) + F_2(\text{HONO}). \quad (5)$$

282

283 The HONO calculated by Eq. 5 can be applied to an urban photochemical cycle simulation.
284 It is already known that the photolysis of HONO is a major source of OH radicals in the early
285 morning when the OH level is low, and this OH affects daytime O₃ formation through
286 photochemical reactions with VOCs and NO_x, which are primarily emitted during morning rush
287 hour in urban areas. In addition, the OH produced from HONO promotes the photochemical
288 oxidation of SO₂ and VOCs, leading to aerosol formation. However, the HONO formation
289 mechanism is still poorly understood, hindering O₃ and fine aerosols as well as HONO from
290 being correctly simulated in conventional photochemical models.

291 The 0-Dimension Atmospheric Modelling (F0AM) utilizing the MCM v3.3.1 chemical
292 reaction mechanisms (Wolfe et al., 2016), can be used to simulate the diurnal variation of O₃
293 with the measurements of several reactive gases (NO, NO₂, CO, HCHO, VOCs, and HONO).

294 Detailed information about F0AM can be found in
295 (<https://sites.google.com/site/wolfegm/models>) and in previous works published elsewhere
296 (Wolfe et al., 2016; Gil et al., 2020). When the F0AM model is run without HONO, it is not
297 able to reproduce the concentration and diel cycle of the observed O₃ (Figure 9). In comparison,
298 the model simulates the O₃ well within 2 ppbv when adding HONO, which is the product of
299 RND v1.0. This is mainly due to the missing OH produced by HONO photolysis in the early
300 morning. Its production rate is estimated to be 0.57 pptv s⁻¹, contributing approximately 2.28
301 pptv to OH budget during 06:00 ~ 11:00 (LST) (Gil et al., 2021). Given that OH is mainly
302 produced from the photolysis of O₃ under high sun, the early morning source of OH will
303 expedite the photochemical cycle involving NO_x and VOCs, promoting O₃ and secondary
304 aerosol formation. Since the presence of HONO in the photochemical model allows for accurate
305 estimation of OH radicals, the incorporation of RNDv1.0 into conventional models will
306 improve their overall performance.

307

308 **4. Summary and implications**

309

310 In this study, we developed the RND model to calculate the mixing ratio of NO_y in an urban
311 atmosphere using a DNN along with measurement data. The target species of RNDv1.0 is
312 HONO, and its mixing ratio is calculated using criteria pollutants including O₃, NO₂, CO, and
313 SO₂, and meteorological variables including T, RH, WS, and WD, along with the SZA. These
314 variables are routinely measured through monitoring networks. The RNDv1.0 was trained and
315 validated using the HONO measurements obtained in Seoul by adopting a k-fold cross
316 validation method and tested with other HONO datasets measured using the same instrument.
317 The validation and test results demonstrate that RNDv1.0 adequately captures the characteristic
318 variation of HONO and confirms the efficacy of RND v1.0.

319 RNDv1.0 was constructed using the measurement made in a high NO_x environment during
320 early summer (May–June). It is noteworthy that in this period, the HONO mixing ratio was
321 raised above 3 ppbv with the highest O₃ levels under stagnant conditions. If RNDv1.0 is applied
322 to areas under significant influence of outflows, the model possibly overestimates or
323 underestimate the level of HONO without detailed information such as nanoparticles. In the

324 previous study, the formation of HONO was shown to be intimately related with surface areas
325 of submicron particles (Gil et al., 2021). Nevertheless, the HONO concentration produced from
326 RNDv1.0 with routine measurements provides the benefit of relatively inexpensive test for
327 measurement quality control, location selection, and supports the data used for traditional
328 chemistry model based on the current knowledge of the urban photochemical cycle. Therefore,
329 it is reasonable to argue that RNDv1.0 can serve as a supplementary tool for conventional
330 forecasting models. As attempts are currently being made to estimate ground HONO from
331 satellite observations (Clarisse et al., 2011;Theys et al., 2020;Armante et al., 2021), RNDv1.0
332 will also be useful for validating satellite-derived HONO by supplementing measurement data.

333

334 **5. Acknowledgements**

335

336 This study was supported by the National Research Foundation of Republic of Korea
337 (2020R1A2C3014592) and Korea Institute of Science and Technology (KIST2E31650-22-
338 P019).

339

340 **6. Code availability**

341

342 The RND model codes (.h5 files) with preprocessed sample data can be downloaded from
343 (Gil, 2021).

344

345 **7. Author contributions**

346

347 JG and ML designed the manuscript and developed the model code. JK, GL, and JA
348 provided HONO measurements and CK provided CMAQ model data. All the authors
349 contributed to the manuscript.

350

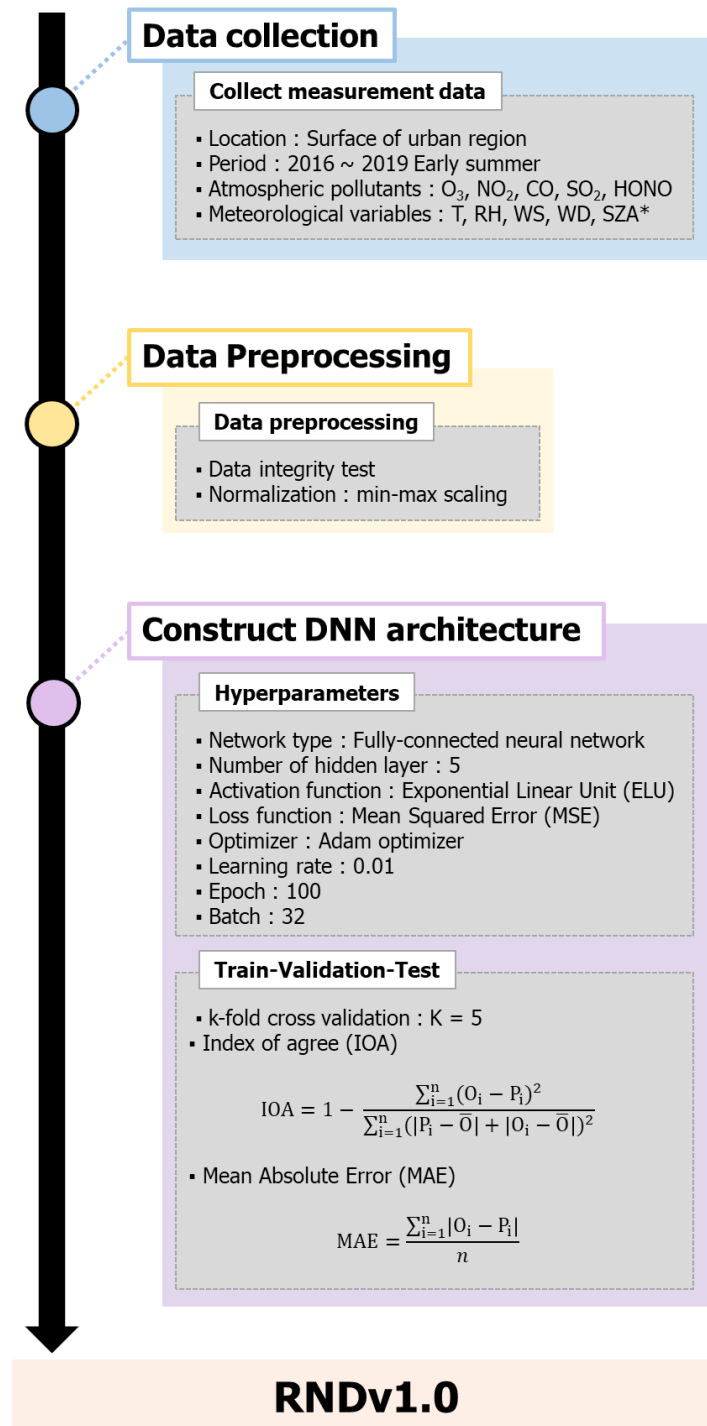
351 **8. Competing interests**

352

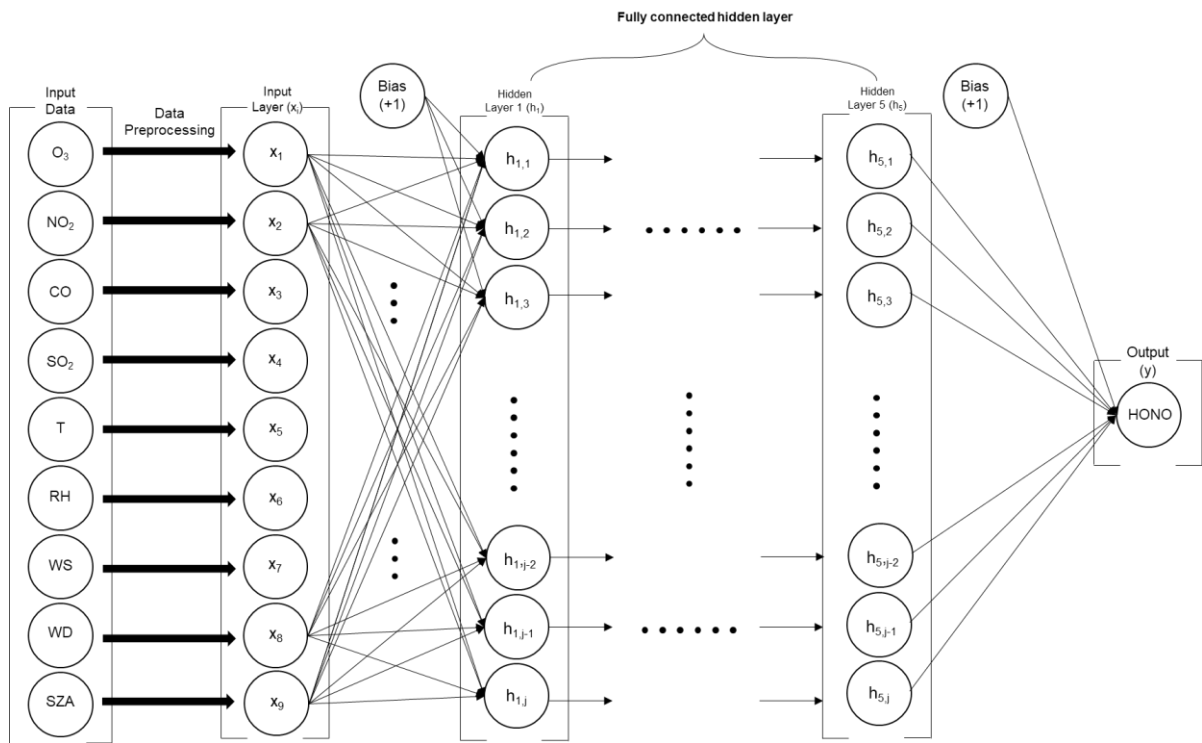
353 The authors declare that they have no conflict of interest.

354

355



359 **Figure 1.** The main processes for configuring the RNDv1.0 (*: calculated values)

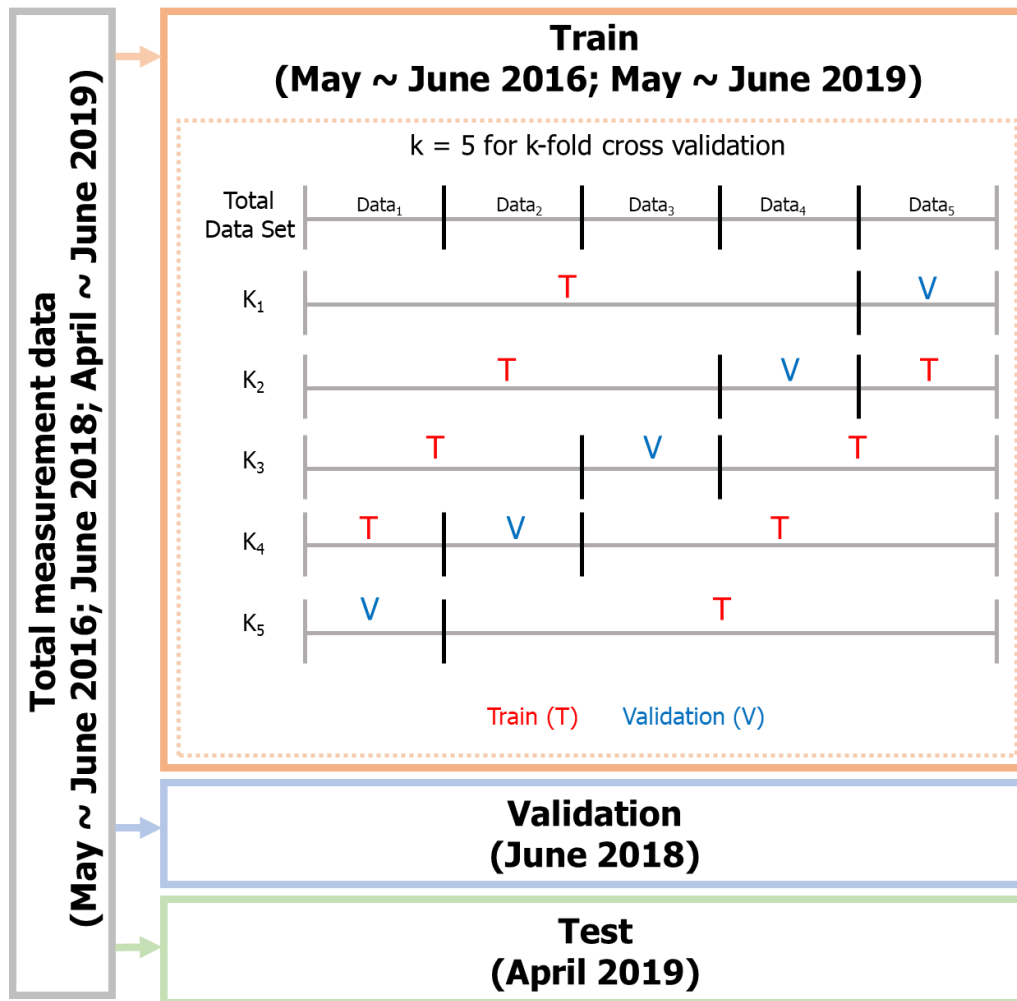


360

361 **Figure 2.** The structure of deep neural network built for RND v1.0.

362

363

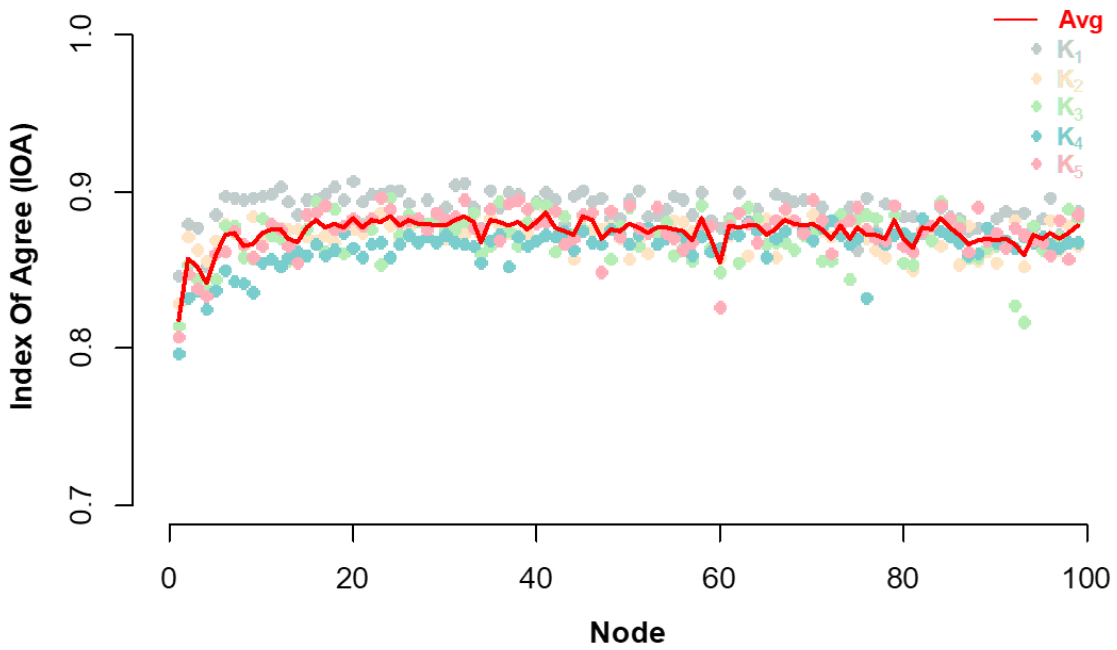


364

365 **Figure 3.** Design of training, validation, and test to build RNDv1.0 using measurement data.

366 The k-fold cross validation were performed using randomly divided five subsets of training data
367 set.

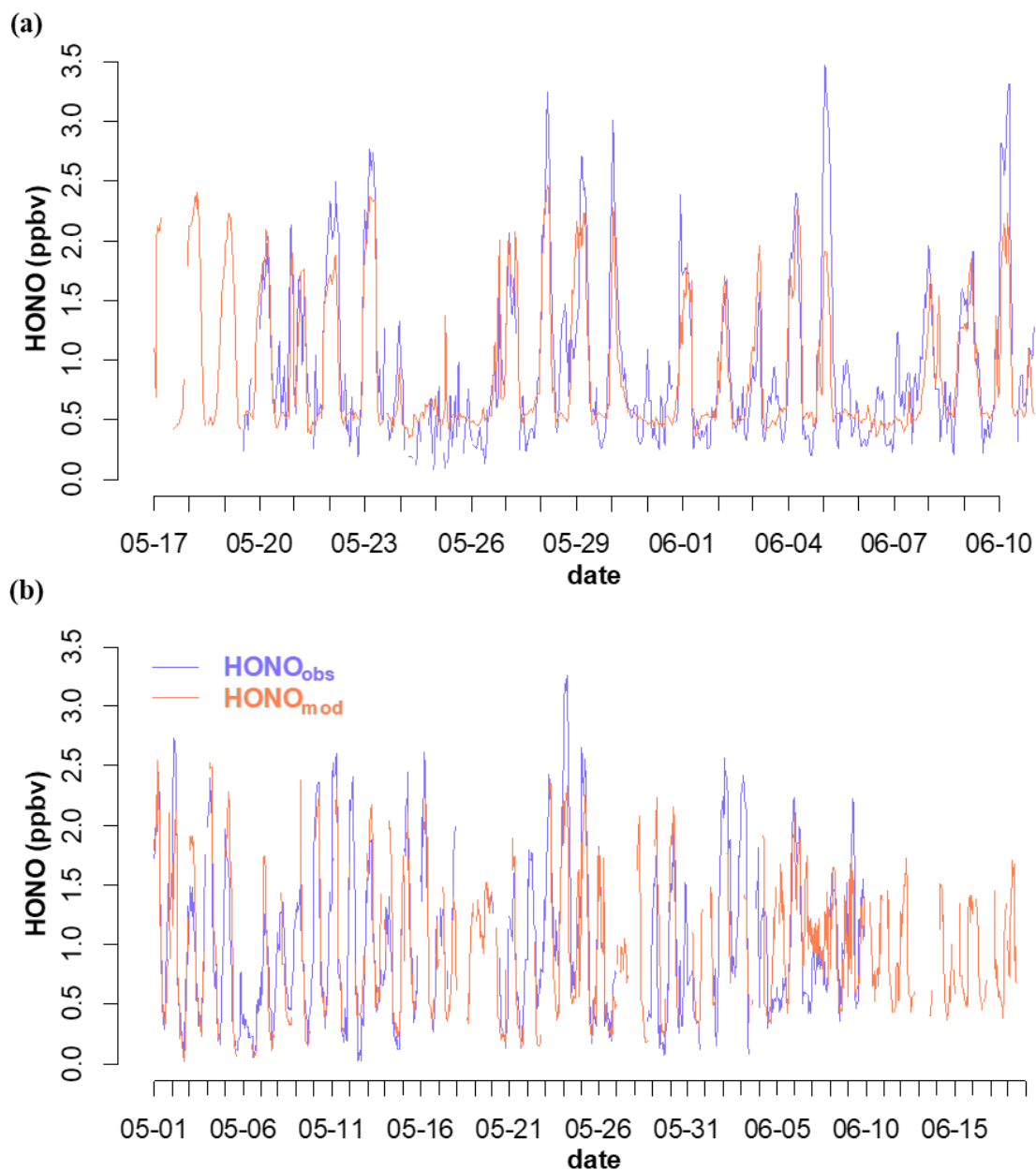
368



369

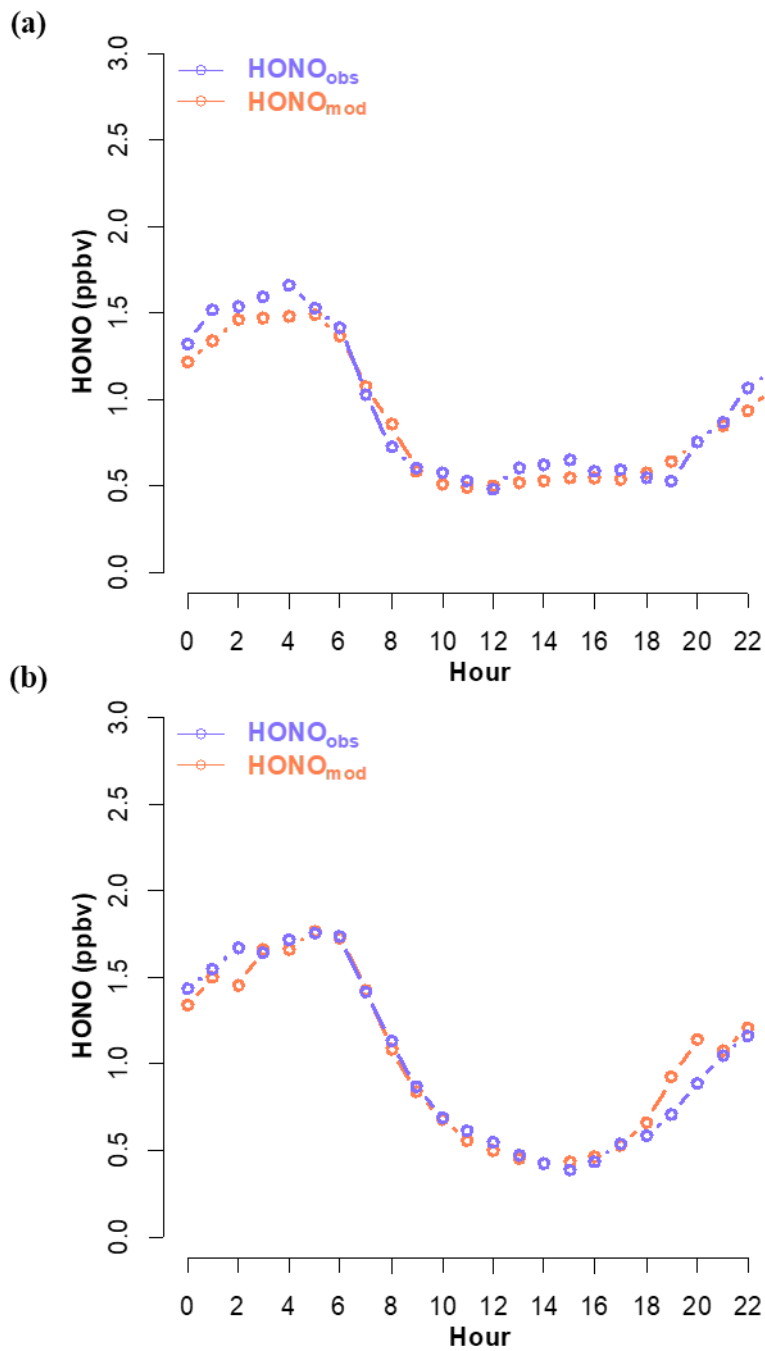
370 **Figure 4.** Index Of Agreement (IOA) for k-fold cross validation. Solid circle and red line
 371 represent IOA for each validation (k=5) and the average of 5 validation sets at each node number.

372



373
 374 **Figure 5.** Comparison between the measured (HONO_{obs}) and calculated (HONO_{mod}) HONO
 375 mixing ratios in Seoul during May~June in (a) 2016 and (b) 2019. The blue and red lines
 376 indicate the measured and calculated HONO mixing ratio, respectively.

377

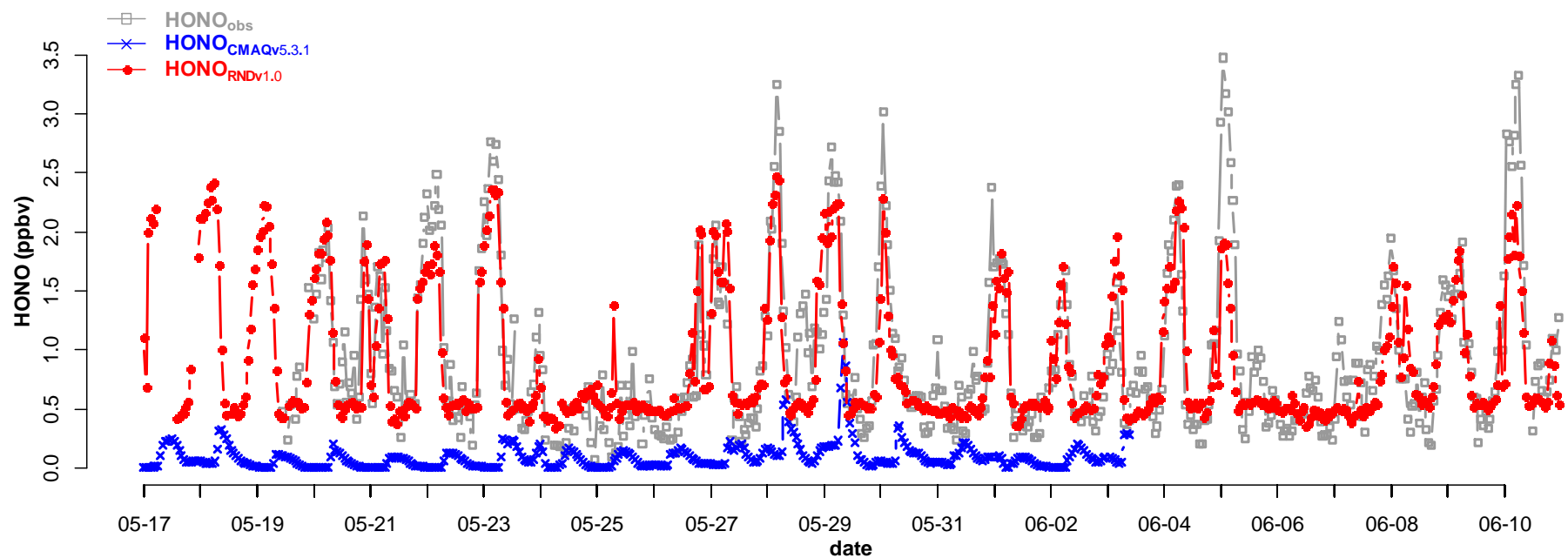


378

379 **Figure 6.** Average diurnal variations of the measured (HONO_{obs}) and the calculated (HONO_{mod})
 380 HONO mixing ratios in Seoul during May ~ June in (a) 2016 and (b) 2019.

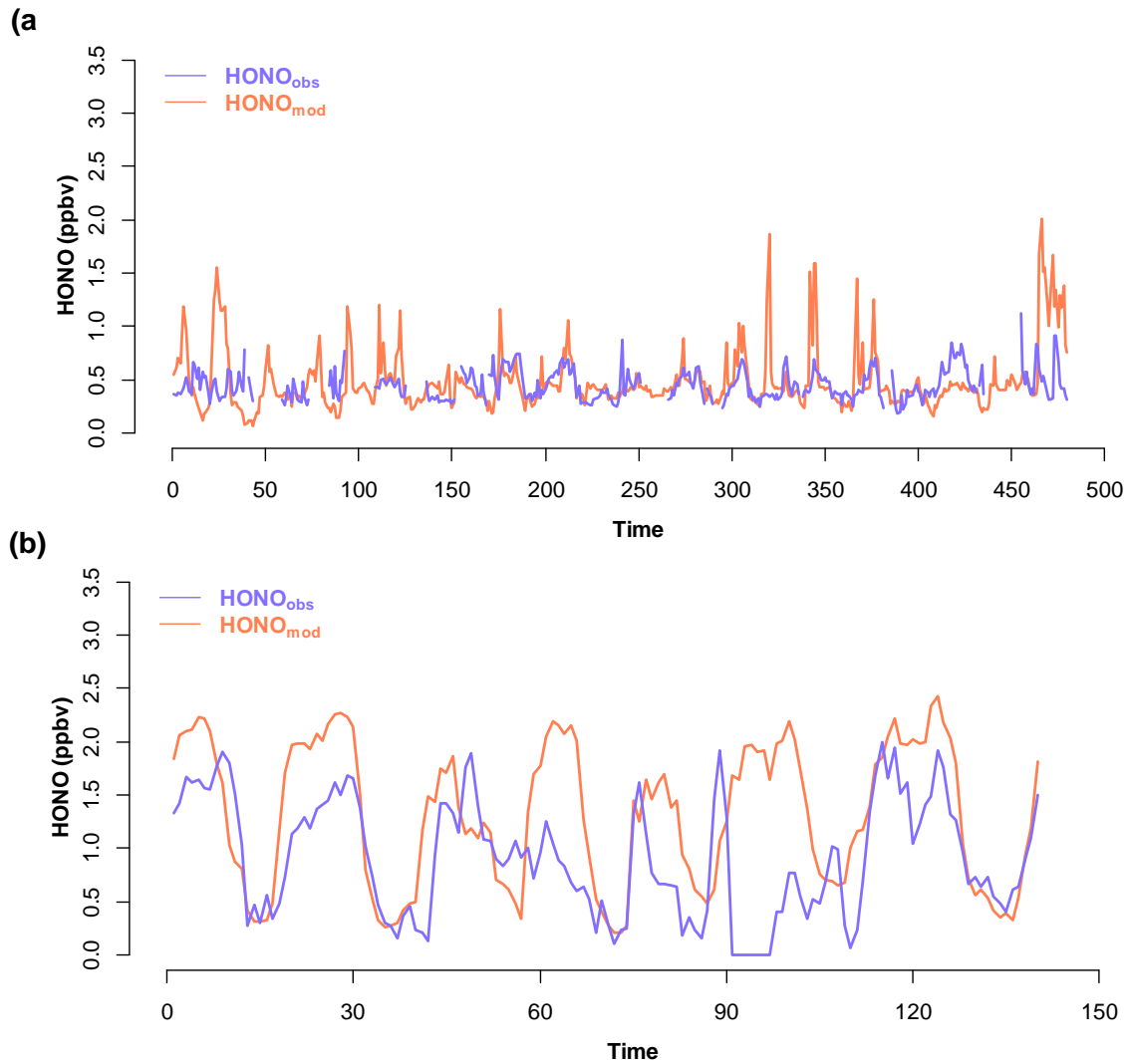
381

382



383

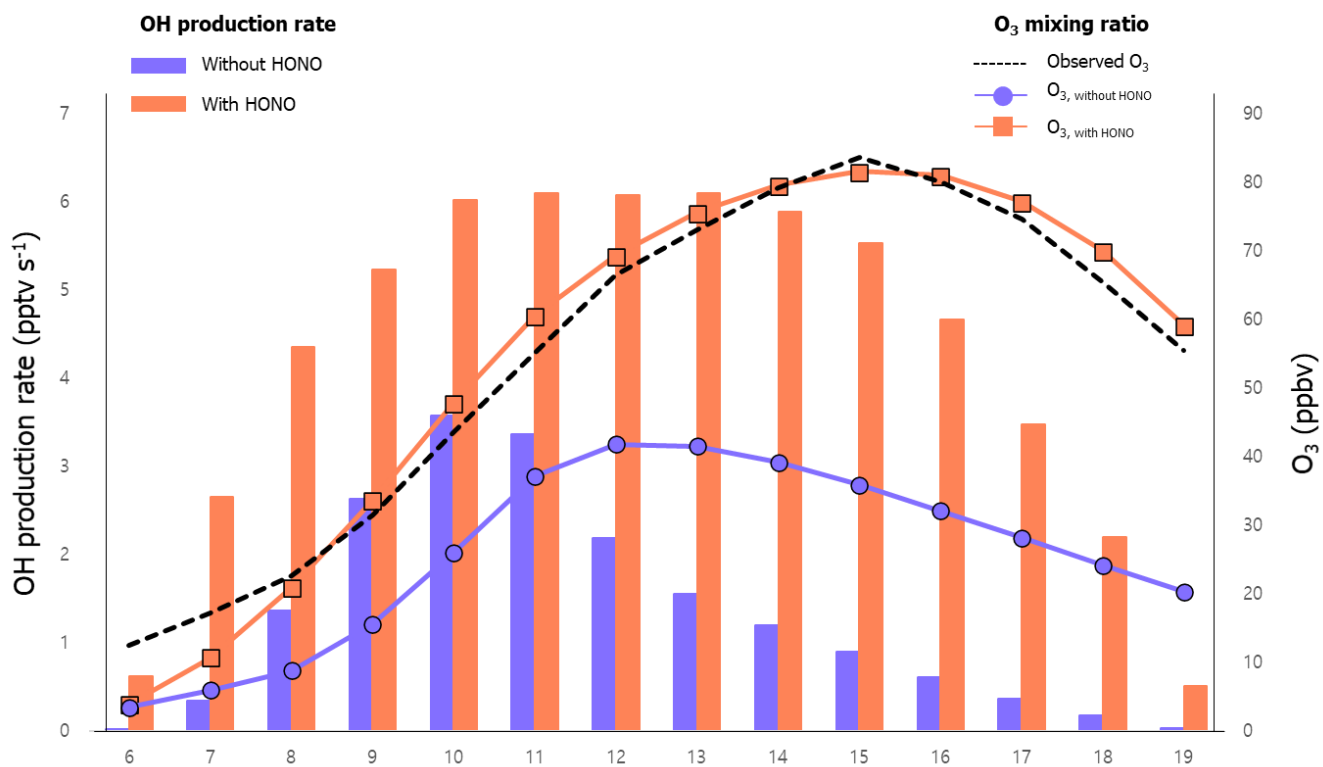
384 **Figure 7.** During the KORUS-AQ campaign (May-June 2016), HONO mixing ratios calculated using RNDv1.0 (red dot) are compared with those
385 observed (gray square) and calculated using CMAQv5.3.1 (blue cross).



386

387 **Figure 8.** Comparison between the measured ($HONO_{obs}$) and calculated ($HONO_{mod}$) HONO
 388 mixing ratios in Seoul during (a) June 2018 and (b) April 2019. The blue and red lines indicate
 389 the measured and calculated HONO mixing ratio, respectively. The x axis indicates the hour
 390 from the beginning of the experiment, which is (a) 00:00 on 1st June 2018 and (b) 00:00 on 12th
 391 April 2019.

392



393

394 **Figure 9.** For June 2016, diurnal variations of O₃ (line) and OH production rate (bar) calculated
 395 from the F0AM photochemical model with (orange) and without (blue) HONO estimated from
 396 the RNDv1.0 model. The measured O₃ is compared with the calculated.

397

398 **Table 1.** Resources for constructing RND model.

	Version	Remark
Python	v3.8.3	
CUDA	v10.1	*If using GPU
CuDNN	v7.6.5	*If using GPU
Tensorflow	v2.3.0	<i>Python library</i>
Keras	v2.4.3	<i>Python library</i>
Pandas	v1.0.5	<i>Python library</i>
Numpy	v1.18.5	<i>Python library</i>

399 *GPU denotes graphic processing unit

400 **Table 2.** Input variables and their concentrations (10th ~ 90th percentile), coverage, and scale
 401 factors for RNDv1.0 model. Measurements were made in Seoul during May ~ June in 2016 and
 402 2019.

	10 th ~90 th percentile (unit)	Coverage (%)	Scale Factor1 (F ₁)*	Scale Factor 2 (F ₂)**
Input Variables				
O ₃	12.1 ~ 90.4 (ppbv)	95.5	204.738	0.842
NO ₂	11.0 ~ 48.6 (ppbv)	80.6	79.925	2.375
CO	252 ~ 743 (ppbv)	95.1	975.248	137.253
SO ₂	1.9 ~ 6.4 (ppbv)	95.6	12.479	0.958
Solar Zenith Angle	22.7 ~ 118.4 (°)	100.0	112.317	14.195
Temperature	15.9 ~ 26.7 (°C)	99.4	24.240	8.610
Relative Humidity	29.2 ~ 79.1 (%)	99.4	88.545	10.555
Wind Speed	0.2 ~ 3.7 (m/s)	99.4	7.581	0.005
Wind Direction	45.4 ~ 287.5 (°)	99.4	359.565	0.235
Output Variables				
HONO	0.3 ~ 2.0 (ppbv)	81.1%	3.447	0.013

403 * Maximum – Minimum

404 ** Minimum value

405

406 **Table 3.** The result of validation and test of RNDv1.0 model using measurement data.

Measurement data	Validation		Test	
	MAE (ppbv)	IOA	MAE (ppbv)	IOA
May 2016*	0.26	0.93		
June 2016*	0.29	0.86		
June 2018	0.21	0.79		
April 2019			0.56	0.65
May 2019*	0.26	0.93		
June 2019*	0.36	0.76		

407 *Re-using the data already used for training

408

409 **Table 4.** The result of bootstrap test of measurement data used to train RNDv1.0 model. The
410 greater the MAE, the greater the influence of variable.

Variable (X)	MAE (ppbv)
-	0.28
O ₃	0.29
NO ₂	0.59
CO	0.37
SO ₂	0.34
Solar zenith Angle (SZA)	0.41
Temperature (T)	0.52
Relative humidity (RH)	0.52
Wind speed (WS)	0.34
Wind direction (WD)	0.29

411

412

413 **Reference**

414

415 Akimoto, H., Nagashima, T., Li, J., Fu, J. S., Ji, D., Tan, J., and Wang, Z.: Comparison of surface
416 ozone simulation among selected regional models in MICS-Asia III—effects of chemistry and
417 vertical transport for the causes of difference, *Atmospheric Chemistry and Physics*, 19, 603-
418 615, 2019.

419 Akimoto, H., and Tanimoto, H.: Review of Comprehensive Measurements of Speciated NO_y
420 and its Chemistry: Need for Quantifying the Role of Heterogeneous Processes of HNO₃ and
421 HONO, *Aerosol and Air Quality Research*, 21, 200395, 2021.

422 Anderson, D. C., Loughner, C. P., Diskin, G., Weinheimer, A., Canty, T. P., Salawitch, R. J.,
423 Worden, H. M., Fried, A., Mikoviny, T., and Wisthaler, A.: Measured and modeled CO and NO_y
424 in DISCOVER-AQ: An evaluation of emissions and chemistry over the eastern US,
425 *Atmospheric Environment*, 96, 78-87, 2014.

426 Appel, K. W., Bash, J. O., Fahey, K. M., Foley, K. M., Gilliam, R. C., Hogrefe, C., Hutzell, W.
427 T., Kang, D., Mathur, R., and Murphy, B. N.: The Community Multiscale Air Quality (CMAQ)
428 model versions 5.3 and 5.3. 1: system updates and evaluation, *Geoscientific Model
429 Development*, 14, 2867-2897, 2021.

430 Arcomano, T., Szunyogh, I., Wikner, A., Pathak, J., Hunt, B. R., and Ott, E.: A Hybrid Approach
431 to Atmospheric Modeling that Combines Machine Learning with a Physics-Based Numerical
432 Model, *Journal of Advances in Modeling Earth Systems*, e2021MS002712, 2021.

433 Armante, R., Perrin, A., Kwabia Tchana, F., and Manceron, L.: The v4 bands at 11 μ m: linelists
434 for the Trans- and Cis-conformer forms of nitrous acid (HONO) in the 2019 version of the
435 GEISA database, *Molecular Physics*, e1951860, 2021.

436 Arnell, N. W., Lowe, J. A., Challinor, A. J., and Osborn, T. J.: Global and regional impacts of
437 climate change at different levels of global temperature increase, *Climatic Change*, 155, 377-
438 391, 2019.

439 Baek, W.-K., and Jung, H.-S.: Performance Comparison of Oil Spill and Ship Classification
440 from X-Band Dual- and Single-Polarized SAR Image Using Support Vector Machine, Random
441 Forest, and Deep Neural Network, *Remote Sensing*, 13, 3203, 2021.

442 Bao, F., Cheng, Y., Kuhn, U., Li, G., Wang, W., Kratz, A. M., Weber, J., Weber, B., Pöschl, U.,
443 and Su, H.: Key Role of Equilibrium HONO Concentration over Soil in Quantifying Soil-
444 Atmosphere HONO Fluxes, *Environmental science & technology*, 2022.

445 Bengio, Y., and Grandvalet, Y.: No unbiased estimator of the variance of K-fold cross-validation,
446 *Citeseer*, 2003.

447 Bloss, W. J., Kramer, L., Crilley, L. R., Vu, T., Harrison, R. M., Shi, Z., Lee, J. D., Squires, F.
448 A., Whalley, L. K., and Slater, E.: Insights into air pollution chemistry and sulphate formation
449 from nitrous acid (HONO) measurements during haze events in Beijing, *Faraday Discussions*,
450 226, 223-238, 2021.

451 Brown, S. S., An, H., Lee, M., Park, J.-H., Lee, S.-D., Fibiger, D. L., McDuffie, E. E., Dubé,
452 W. P., Wagner, N. L., and Min, K.-E.: Cavity enhanced spectroscopy for measurement of
453 nitrogen oxides in the Anthropocene: results from the Seoul tower during MAPS 2015, *Faraday
454 discussions*, 200, 529-557, 2017.

455 Canty, T., Hembeck, L., Vinciguerra, T., Anderson, D., Goldberg, D., Carpenter, S., Allen, D.,
456 Loughner, C., Salawitch, R., and Dickerson, R.: Ozone and NO_x chemistry in the eastern US:
457 evaluation of CMAQ/CB05 with satellite (OMI) data, *Atmospheric Chemistry and Physics*, 15,
458 10965-10982, 2015.

459 Chen, G., Li, S., Knibbs, L. D., Hamm, N. A., Cao, W., Li, T., Guo, J., Ren, H., Abramson, M.
460 J., and Guo, Y.: A machine learning method to estimate PM_{2.5} concentrations across China
461 with remote sensing, meteorological and land use information, *Science of the Total*
462 *Environment*, 636, 52-60, 2018a.

463 Chen, Y., Wolke, R., Ran, L., Birmili, W., Spindler, G., Schröder, W., Su, H., Cheng, Y., Tegen,
464 I., and Wiedensohler, A.: A parameterization of the heterogeneous hydrolysis of N₂O₅ for mass-
465 based aerosol models: improvement of particulate nitrate prediction, *Atmos. Chem. Phys.*, 18,
466 673-689, 2018b.

467 Cheng, P., Pour-Biazar, A., White, A. T., and McNider, R. T.: Improvement of summertime
468 surface ozone prediction by assimilating Geostationary Operational Environmental Satellite
469 cloud observations, *Atmospheric Environment*, 268, 118751, 2022.

470 Clarisse, L., R'Honi, Y., Coheur, P. F., Hurtmans, D., and Clerbaux, C.: Thermal infrared nadir
471 observations of 24 atmospheric gases, *Geophysical Research Letters*, 38, 2011.

472 Cui, L., and Wang, S.: Mapping the daily nitrous acid (HONO) concentrations across China
473 during 2006-2017 through ensemble machine-learning algorithm, *Science of The Total*
474 *Environment*, 147325, 2021.

475 Dang, C., Liu, Y., Yue, H., Qian, J., and Zhu, R.: Autumn crop yield prediction using data-driven
476 approaches:-support vector machines, random forest, and deep neural network methods,
477 *Canadian Journal of Remote Sensing*, 47, 162-181, 2021.

478 Ding, B., Qian, H., and Zhou, J.: Activation functions and their characteristics in deep neural
479 networks, 2018 Chinese control and decision conference (CCDC), 2018, 1836-1841.

480 Ge, B., Xu, X., Ma, Z., Pan, X., Wang, Z., Lin, W., Ouyang, B., Xu, D., Lee, J., and Zheng, M.:
481 Role of Ammonia on the Feedback Between AWC and Inorganic Aerosol Formation During
482 Heavy Pollution in the North China Plain, *Earth and Space Science*, 6, 1675-1693, 2019.

483 Gen, M., Liang, Z., Zhang, R., Mabato, B. R. G., and Chan, C. K.: Particulate nitrate photolysis
484 in the atmosphere, *Environmental Science: Atmospheres*, 2022.

485 Gil, J., Son, J., Kang, S., Park, J., Lee, M., Jeon, E., and Shim, M.: HONO measurement in
486 Seoul during Summer 2018 and its Impact on Photochemistry, *Journal of Korean Society for*
487 *Atmospheric Environment*, 36, 579-588, 10.5572/KOSAE.2020.36.5.579, 2020.

488 Gil, J.: RNDv1.0 and example, <https://doi.org/10.5281/zenodo.5540180>, in, Zenodo, 2021.

489 Gil, J., Kim, J., Lee, M., Lee, G., Ahn, J., Lee, D. S., Jung, J., Cho, S., Whitehill, A., Szykman,
490 J., and Lee, J.: Characteristics of HONO and its impact on O₃ formation in the Seoul
491 Metropolitan Area during the Korea-US Air Quality study, *Atmospheric Environment*, 2021,
492 <https://doi.org/10.1016/j.atmosenv.2020.118182>., 2021.

493 Gu, R., Wang, W., Peng, X., Xia, M., Zhao, M., Zhang, Y., Liu, Y., Shen, H., Xue, L., and Wang,
494 T.: Nitrous acid in the polluted coastal atmosphere of the South China Sea: Ship emissions,
495 budgets, and impacts, *Science of The Total Environment*, 153692, 2022.

496 IPCC: Summary for policymakers. In: *Climate Change 2014: Impacts, Adaption, and*
497 *Vulnerability. Part A: Global and Sectoral Aspects. Contribution of Working Group II to the*
498 *Fifth Assessment Report of the Intergovernmental Panel on Climate Change* [Field, C.B., V.R.
499 Barros, D.J. Dokken, K.J. Mach, M.D. Mastrandrea, T.E. Bilir, M. Chatterjee, K.L. Ebi, Y.O.
500 Estrada, R.C. Genova, B. Girma, E.S. Kissel, A.N. Levy, S. MacCracken, P.R. Mastrandrea,
501 and L.L.White (eds.)], Cambridge, United Kingdom and New York, NY, USA, 1-32, 2014.

502 Jia, C., Tong, S., Zhang, W., Zhang, X., Li, W., Wang, Z., Wang, L., Liu, Z., Hu, B., and Zhao,
503 P.: Pollution characteristics and potential sources of nitrous acid (HONO) in early autumn 2018
504 of Beijing, *Science of The Total Environment*, 735, 139317, 2020.

505 Jordan, C., Crawford, J. H., Beyersdorf, A. J., Eck, T. F., Halliday, H. S., Nault, B. A., Chang,
506 L.-S., Park, J., Park, R., Lee, G., Kim, H., Ahn, J.-y., Cho, S., Shin, H. J., Lee, J. H., Jung, J.,

507 Kim, D.-S., Lee, M., Lee, T., Whitehill, A., Szykman, J., Schueneman, M. K., Campuzano-Jost,
508 P., Jimenez, J. L., DiGangi, J. P., Diskin, G. S., Anderson, B. E., Moore, R. H., Ziemba, L. D.,
509 Fenn, M. A., Hair, J. W., Kuehn, R. E., Holz, R. E., Chen, G., Travis, K., Shook, M., Peterson,
510 D. A., Lamb, K. D., and Schwarz, J. P.: Investigation of factors controlling PM_{2.5} variability
511 across the South Korean Peninsula during KORUS-AQ, *Elementa: Science of the*
512 *Anthropocene*, in review, 2020.

513 Joutsensaari, J., Ozon, M., Nieminen, T., Mikkonen, S., Lähivaara, T., Decesari, S., Facchini,
514 M. C., Laaksonen, A., and Lehtinen, K. E.: Identification of new particle formation events with
515 deep learning, *Atmospheric Chemistry and Physics*, 18, 9597-9615, 2018.

516 Kang, Y., Choi, H., Im, J., Park, S., Shin, M., Song, C.-K., and Kim, S.: Estimation of surface-
517 level NO₂ and O₃ concentrations using TROPOMI data and machine learning over East Asia,
518 *Environmental Pollution*, 288, 117711, 2021.

519 Kim, H., Gil, J., Lee, M., Jung, J., Whitehill, A., Szykman, J., Lee, G., Kim, D., Cho, S., Ahn,
520 J., Hong, J., and Park, M.: Overview and characteristics of air quality in the Seoul Metropolitan
521 Area during the KORUS-AQ campaign, *Elementa: Science of the Anthropocene*, in review,
522 2020.

523 Kleffmann, J., Lörzer, J., Wiesen, P., Kern, C., Trick, S., Volkamer, R., Rodenas, M., and Wirtz,
524 K.: Intercomparison of the DOAS and LOPAP techniques for the detection of nitrous acid
525 (HONO), *Atmospheric Environment*, 40, 3640-3652, 2006.

526 Kleinert, F., Leufen, L. H., and Schultz, M. G.: IntelliO₃-ts v1. 0: a neural network approach to
527 predict near-surface ozone concentrations in Germany, *Geoscientific Model Development*, 14,
528 1-25, 2021.

529 Krishnamurthy, R., Newsom, R. K., Berg, L. K., Xiao, H., Ma, P.-L., and Turner, D. D.: On the
530 estimation of boundary layer heights: a machine learning approach, *Atmospheric Measurement*
531 *Techniques*, 14, 4403-4424, 2021.

532 Lee, B. H., Wood, E. C., Zahniser, M. S., McManus, J. B., Nelson, D. D., Herndon, S. C.,
533 Santoni, G., Wofsy, S. C., and Munger, J. W.: Simultaneous measurements of atmospheric
534 HONO and NO₂ via absorption spectroscopy using tunable mid-infrared continuous-wave
535 quantum cascade lasers, *Applied Physics B*, 102, 417-423, 2011.

536 Levy, M., Zhang, R., Zheng, J., Zhang, A. L., Xu, W., Gomez-Hernandez, M., Wang, Y., and
537 Olaguer, E.: Measurements of nitrous acid (HONO) using ion drift-chemical ionization mass
538 spectrometry during the 2009 SHARP field campaign, *Atmospheric Environment*, 94, 231-240,
539 2014.

540 Li, S., Song, W., Zhan, H., Zhang, Y., Zhang, X., Li, W., Tong, S., Pei, C., Wang, Y., and Chen,
541 Y.: Contribution of Vehicle Emission and NO₂ Surface Conversion to Nitrous Acid (HONO) in
542 Urban Environments: Implications from Tests in a Tunnel, *Environmental Science &*
543 *Technology*, 55, 15616-15624, 2021a.

544 Li, Y., Wang, X., Wu, Z., Li, L., Wang, C., Li, H., Zhang, X., Zhang, Y., Li, J., and Gao, R.:
545 Atmospheric nitrous acid (HONO) in an alternate process of haze pollution and ozone pollution
546 in urban Beijing in summertime: Variations, sources and contribution to atmospheric
547 photochemistry, *Atmospheric Research*, 260, 105689, 2021b.

548 Li, Z., Xie, P., Hu, R., Wang, D., Jin, H., Chen, H., Lin, C., and Liu, W.: Observations of N₂O₅
549 and NO₃ at a suburban environment in Yangtze river delta in China: Estimating heterogeneous
550 N₂O₅ uptake coefficients, *Journal of Environmental Sciences*, 2020.

551 Liebmann, J., Karu, E., Sobanski, N., Schuladen, J., Ehn, M., Schallhart, S., Quéléver, L.,
552 Hellen, H., Hakola, H., and Hoffmann, T.: Direct measurement of NO₃ radical reactivity in a
553 boreal forest, *Atmospheric Chemistry and Physics*, 2018.

554 Liu, Y., Lu, K., Li, X., Dong, H., Tan, Z., Wang, H., Zou, Q., Wu, Y., Zeng, L., and Hu, M.: A
555 comprehensive model test of the HONO sources constrained to field measurements at rural
556 North China Plain, *Environmental science & technology*, 53, 3517-3525, 2019.

557 Mallet, V., and Sportisse, B.: Uncertainty in a chemistry-transport model due to physical
558 parameterizations and numerical approximations: An ensemble approach applied to ozone
559 modeling, *Journal of Geophysical Research: Atmospheres*, 111, 2006.

560 Meng, F., Qin, M., Fang, W., Duan, J., Tang, K., Zhang, H., Shao, D., Liao, Z., Feng, Y., and
561 Huang, Y.: Measurement of HONO flux using the aerodynamic gradient method over an
562 agricultural field in the Huaihe River Basin, China, *Journal of Environmental Sciences*, 2022.

563 Monks, P. S., Archibald, A., Colette, A., Cooper, O., Coyle, M., Derwent, R., Fowler, D.,
564 Granier, C., Law, K. S., and Mills, G.: Tropospheric ozone and its precursors from the urban to
565 the global scale from air quality to short-lived climate forcer, *Atmospheric Chemistry and
566 Physics*, 15, 8889-8973, 2015.

567 Myhre, G., Aas, W., Cherian, R., Collins, W., Faluvegi, G., Flanner, M., Forster, P., Hodnebrog,
568 Ø., Klimont, Z., and Lund, M. T.: Multi-model simulations of aerosol and ozone radiative
569 forcing due to anthropogenic emission changes during the period 1990–2015, *Atmospheric
570 Chemistry and Physics*, 17, 2709-2720, 2017.

571 Peterson, D. A., Hyer, E. J., Han, S.-O., Crawford, J. H., Park, R. J., Holz, R., Kuehn, R. E.,
572 Eloranta, E., Knute, C., and Jordan, C. E.: Meteorology influencing springtime air quality,
573 pollution transport, and visibility in Korea, *Elem Sci Anth*, 7, 2019.

574 Pinto, J., Dibb, J., Lee, B., Rappenglück, B., Wood, E., Levy, M., Zhang, R. Y., Lefer, B., Ren,
575 X. R., and Stutz, J.: Intercomparison of field measurements of nitrous acid (HONO) during the
576 SHARP campaign, *Journal of Geophysical Research: Atmospheres*, 119, 5583-5601, 2014.

577 Reichstein, M., Camps-Valls, G., Stevens, B., Jung, M., Denzler, J., and Carvalhais, N.: Deep
578 learning and process understanding for data-driven Earth system science, *Nature*, 566, 195-204,
579 2019.

580 Roberts, J. M., Veres, P., Warneke, C., Neuman, J., Washenfelder, R., Brown, S., Baasandorj,
581 M., Burkholder, J., Burling, I., and Johnson, T. J.: Measurement of HONO, HNCO, and other
582 inorganic acids by negative-ion proton-transfer chemical-ionization mass spectrometry (NI-PT-
583 CIMS): Application to biomass burning emissions, *Atmospheric Measurement Techniques*, 3,
584 981, 2010.

585 Schultz, M., Betancourt, C., Gong, B., Kleinert, F., Langguth, M., Leufen, L., Mozaffari, A.,
586 and Stadtler, S.: Can deep learning beat numerical weather prediction?, *Philosophical
587 Transactions of the Royal Society A*, 379, 20200097, 2021.

588 Shahriar, S. A., Kayes, I., Hasan, K., Salam, M. A., and Chowdhury, S.: Applicability of
589 machine learning in modeling of atmospheric particle pollution in Bangladesh, *Air Quality,
590 Atmosphere & Health*, 13, 1247-1256, 2020.

591 Shareef, M. M., Husain, T., and Alharbi, B.: Studying the Effect of Different Gas-Phase
592 Chemical Kinetic Mechanisms on the Formation of Oxidants, Nitrogen Compounds and Ozone
593 in Arid Regions, *Journal of Environmental Protection*, 10, 1006-1031, 2019.

594 Shindell, D. T., Lamarque, J.-F., Schulz, M., Flanner, M., Jiao, C., Chin, M., Young, P., Lee, Y.
595 H., Rotstayn, L., and Mahowald, N.: Radiative forcing in the ACCMIP historical and future
596 climate simulations, *Atmospheric Chemistry and Physics*, 13, 2939-2974, 2013.

597 Stadtler, S., Simpson, D., Schröder, S., Taraborrelli, D., Bott, A., and Schultz, M.: Ozone
598 impacts of gas–aerosol uptake in global chemistry transport models, *Atmospheric chemistry
599 and physics*, 18, 3147-3171, 2018.

600 Stevenson, D., Young, P., Naik, V., Lamarque, J.-F., Shindell, D. T., Voulgarakis, A., Skeie, R.
601 B., Dalsoren, S. B., Myhre, G., and Berntsen, T. K.: Tropospheric ozone changes, radiative

602 forcing and attribution to emissions in the Atmospheric Chemistry and Climate Model
603 Intercomparison Project (ACCMIP), *Atmospheric Chemistry and Physics*, 13, 3063-3085, 2013.

604 Sumathi, S., and Pugalendhi, G. K.: Cognition based spam mail text analysis using combined
605 approach of deep neural network classifier and random forest, *Journal of Ambient Intelligence*
606 and *Humanized Computing*, 12, 5721-5731, 2021.

607 Sun, Y., Wang, L., Wang, Y., Quan, L., and Zirui, L.: In situ measurements of SO₂, NO_x, NO_y,
608 and O₃ in Beijing, China during August 2008, *Science of the Total Environment*, 409, 933-940,
609 2011.

610 Theys, N., Volkamer, R., Müller, J.-F., Zarzana, K. J., Kille, N., Clarisse, L., De Smedt, I., Lerot,
611 C., Finkenzeller, H., and Hendrick, F.: Global nitrous acid emissions and levels of regional
612 oxidants enhanced by wildfires, *Nature geoscience*, 13, 681-686, 2020.

613 Tie, X., Geng, F., Guenther, A., Cao, J., Greenberg, J., Zhang, R., Apel, E., Li, G., Weinheimer,
614 A., and Chen, J.: Megacity impacts on regional ozone formation: observations and WRF-Chem
615 modeling for the MIRAGE-Shanghai field campaign, *Atmospheric Chemistry and Physics*, 13,
616 5655-5669, 2013.

617 VandenBoer, T., Markovic, M., Sanders, J., Ren, X., Pusede, S., Browne, E., Cohen, R., Zhang,
618 L., Thomas, J., and Brune, W. H.: Evidence for a nitrous acid (HONO) reservoir at the ground
619 surface in Bakersfield, CA, during CalNex 2010, *Journal of Geophysical Research:*
620 *Atmospheres*, 119, 9093-9106, 2014.

621 Varotsos, K., Giannakopoulos, C., and Tombrou, M.: Assessment of the Impacts of climate
622 change on european ozone levels, *Water, Air, & Soil Pollution*, 224, 1-13, 2013.

623 Wang, H., Chen, X., Lu, K., Hu, R., Li, Z., Wang, H., Ma, X., Yang, X., Chen, S., and Dong,
624 H.: NO₃ and N₂O₅ chemistry at a suburban site during the EXPLORE-YRD campaign in 2018,
625 *Atmospheric Environment*, 224, 117180, 2020.

626 Wang, T., Qin, Z., and Zhu, M.: An ELU network with total variation for image denoising,
627 *International Conference on Neural Information Processing*, 2017a, 227-237.

628 Wang, X., Wang, H., Xue, L., Wang, T., Wang, L., Gu, R., Wang, W., Tham, Y. J., Wang, Z.,
629 and Yang, L.: Observations of N₂O₅ and ClNO₂ at a polluted urban surface site in North China:
630 High N₂O₅ uptake coefficients and low ClNO₂ product yields, *Atmospheric environment*, 156,
631 125-134, 2017b.

632 Wolfe, G. M., Marvin, M. R., Roberts, S. J., Travis, K. R., and Liao, J.: The framework for 0-
633 D atmospheric modeling (F0AM) v3. 1, *Geoscientific Model Development*, 9, 3309, 2016.

634 Xu, Z., Liu, Y., Nie, W., Sun, P., Chi, X., and Ding, A.: Evaluating the measurement interference
635 of wet rotating-denuder-ion chromatography in measuring atmospheric HONO in a highly
636 polluted area, *Atmospheric Measurement Techniques*, 12, 6737-6748, 2019.

637 Xue, C., Ye, C., Ma, Z., Liu, P., Zhang, Y., Zhang, C., Tang, K., Zhang, W., Zhao, X., and Wang,
638 Y.: Development of stripping coil-ion chromatograph method and intercomparison with CEAS
639 and LOPAP to measure atmospheric HONO, *Science of The Total Environment*, 646, 187-195,
640 2019.

641 Ye, C., Zhou, X., Pu, D., Stutz, J., Festa, J., Spolaor, M., Tsai, C., Cantrell, C., Mauldin, R. L.,
642 and Campos, T.: Rapid cycling of reactive nitrogen in the marine boundary layer, *Nature*, 532,
643 489-491, 2016.

644